Nanoscale Advances

ROYAL SOCIETY OF CHEMISTRY

PAPER

View Article Online
View Journal | View Issue



Cite this: *Nanoscale Adv.*, 2020, **2**, 5699

# Scalable colloidal synthesis of $Bi_2Te_{2.7}Se_{0.3}$ plate-like particles give access to a high-performing n-type thermoelectric material for low temperature application†

Nagendra S. Chauhan, *[a] Oleg I. Lebedev,[b] Kirill Kovnir, [cd] Sergey V. Pyrlin, [e] Luis S. A. Marques,[e] Marta M. D. Ramos, [e] Brian A. Korgel[f] and Yury V. Kolen'ko *[a]

Colloidal synthesis is harnessed for the gram-scale preparation of hexagonal-shaped plate-like $Bi_2Te_{2.7}Se_{0.3}$ particles, yielding nearly 5 g of the product in one experiment. The resultant textured particles are highly crystalline, phase-pure, chemically uniform, and can serve as a starting material for the preparation of bulk thermoelectrics for room temperature applications. The consolidation occurs *via* spark plasma sintering, which affords nanostructured n-type $Bi_2Te_{2.7}Se_{0.3}$ material exhibiting a high figure of merit $ZT \approx 1$ at 373 K with an average $ZT \approx 0.93$ (300–473 K). Our experimental and theoretical studies indicate that the high thermoelectric performance is attributed to a favorable combination of the resultant transport properties. Specifically, bottom-up formation of the plate-like particles results in the substantial reduction of thermal conductivity by nanostructuring as observed experimentally and can be ascribed to phonon scattering at grain boundaries and suppressed bipolar conduction. When coupled with high electrical conductivity, which is preserved at the bulk scale as confirmed by *ab initio* calculations, these factors boost the thermoelectric performance of the as-synthesized n-type $Bi_2Te_{2.7}Se_{0.3}$ bulk nanostructured alloy to the state-of-the-art level. The combination of a newly developed scalable colloidal synthesis with optimized spark plasma sintering constitutes a convenient route to nanostructured bulk thermoelectrics, which is an interesting pathway for the preparation of simple and complex thermoelectric chalcogenides.

Received 21st August 2020
Accepted 31st October 2020

DOI: 10.1039/d0na00691b

rsc.li/nanoscale-advances



## 1. Introduction

The economic viability of thermoelectric (TE) technology continues to majorly impede its widespread applicability.[1] This is primarily due to the relatively low energy conversion efficiency of TEs coupled with high fabrication costs. Thus, ongoing research for the commercialization of TE devices is mostly driven in two directions: (i) enhancing the performance of the TE materials by optimizing the transport properties and (ii) improving the synthesis methods for reduced cost and scalability. The dimensionless TE figure-of-merit ($ZT$) is a fundamental parameter used to evaluate the TE transport properties of p and n-type thermoelements, which is expressed as $ZT = \left(\frac{\alpha^2\sigma}{\kappa}\right)T$; where $\alpha$, $\sigma$, and $\kappa$ represent the Seebeck coefficient, electrical conductivity, and thermal conductivity at the absolute temperature ($T$), respectively.[2–4] These thermoelements accompanying metallic interconnects are arranged as an array of thermocouples to form a TE device.

For almost seven decades, materials based on bismuth telluride, $Bi_2Te_3$, have led the pursuit for high $ZT$ at near room-temperature.[5,6] They are widely used nowadays in commercialized Peltier devices operational in this temperature regime for practical cooling applications and appear promising to power ubiquitous sensors and wearable devices in the future.[7–10] As an n-type narrow band semiconductor, $Bi_2Te_3$ crystallizes in the tetradymite $Bi_2Te_2S$-type structure with rhombohedral symmetry, and exhibits very high $ZT$ values in the lower temperature range of 300–500 K.[11,12] In bulk $Bi_2Te_3$, using isoelectronic dopants, Sb at the Bi-site as $(Bi_{1-x}Sb_x)_2Te_3$ for p-type[13,14] and Se at the Te-site as $Bi_2(Te_{1-x}Se_x)_3$ for n-type,[15–22] the most effective substitution was found to be $Bi_{0.5}Sb_{1.5}Te_3$ and

[a]International Iberian Nanotechnology Laboratory (INL), Braga 4715-330, Portugal. E-mail: nagendra599@gmail.com; yury.kolenko@inl.int; Fax: +351 253 140 119; Tel: +351 253 140 112, ext. 2534

[b]Laboratoire CRISMAT, UMR 6508, CNRS-Ensicaen, Caen 14050, France

[c]Department of Chemistry, Iowa State University, Ames, Iowa 50011, USA

[d]Ames Laboratory, U.S. Department of Energy, Ames, Iowa 50011, USA

[e]Centro de Física das Universidades do Minho e do Porto, Universidade do Minho, Braga, 4710-057, Portugal

[f]McKetta Department of Chemical Engineering, The University of Texas at Austin, Austin, Texas 78712, USA

† Electronic supplementary information (ESI) available. See DOI: 10.1039/d0na00691b

$Bi_2Te_{2.7}Se_{0.3}$, exhibiting desirable transport properties and the best *ZT*.[6]

The advent of nanostructuring techniques and the broadly recognized effect of quantum confinement on TE transport properties[23] have stimulated extensive research on nanostructure formation, which has been explored for $Bi_2Te_3$ [24–26] and its optimal doped compositions[27–32] to decouple the inversely correlated electrical and thermal transport. Accordingly, $Bi_2Te_3$-based nanostructures attained by mechanical alloying,[20–22,28–30] melt spinning,[19,27,33,34] and wet chemical approaches[13–18,24–26] have been reported. Simultaneously, powder metallurgical techniques for bulk fabrication have been improved to prevent grain growth during sintering by applying higher heating rates using spark plasma sintering (SPS) as compared to conventional hot pressing.[35] These strategies have led to an unprecedented boost in TE performance, particularly in p-type $Bi_2Te_3$-based materials, where $ZT > 1$ was widely reported in lower temperature regimes.[13,27,28,33] On the other hand, it has been commonly observed that higher *ZT* in polycrystalline samples of n-type $Bi_2Te_3$ alloys is more difficult to achieve, and these materials are bound to exhibit inferior *ZT* values, resulting in relatively inefficient modules or devices.[6] This is largely due to the difficulties in simultaneously suppressing the intrinsic bipolar conduction and $\kappa$ while maintaining the higher carrier mobility.[6] Thus, significant research efforts have been directed towards *ZT* enhancement of n-type $Bi_2Te_3$-based alloys.[15–22,29–32]

To attain improved performances using low-cost fabrication in optimal $Bi_2Te_{2.7}Se_{0.3}$, unconventional nanostructuring approaches have gained much attention in the recent years.[15–21,29–32] In this context, wet chemical processing is a particularly attractive route for attaining low-dimension nanostructures in a more cost- and energy-effective manner compared to conventional melting-based solid-state reaction methods.[15–18] Recently, we demonstrated a bottom-up colloidal synthesis of high-quality complex metal chalcogenide nanoparticles on a large scale.[36] In the current study, we broaden the scope of this synthesis to produce nanoplatelet (NP) building blocks to form a high performance n-type TE alloy through SPS. A maximum $ZT \approx 1$ at 373 K was obtained in the nanostructured bulk alloy with $ZT_{avg} \approx 0.93$ (300–473 K), making the resultant TE material a promising counterpart of highly efficient and available p-type $Bi_2Te_3$ based alloys. The detailed structural characterization, theoretical calculations, and transport property measurements were correlated to present the synthesized bulk nanostructured $Bi_2Te_{2.7}Se_{0.3}$ alloys for low temperature TE applications.

## 2. Experimental section

### 2.1 Reagents

Hexadecylamine (HDA, 95.0%, TCI), bismuth(III) acetate ($Bi(ac)_3$, 99.99%, Sigma-Aldrich), diphenyl diselenide ($Ph_2Se_2$, 97%, TCI), and diphenyl ditelluride ($Ph_2Te_2$, 97%, Acros Organics) were used as received. Analytical reagent grade absolute ethanol and toluene were obtained from Fisher Scientific.

### 2.2 Colloidal synthesis of $Bi_2Te_{2.7}Se_{0.3}$ particles

The synthesis was carried out using standard Schlenk line techniques. In a typical experiment, HDA (60.0 g, 249 mmol), $Bi(ac)_3$ (4.91 g, 12.7 mmol), $Ph_2Se_2$ (0.328 g, 1.05 mmol), and $Ph_2Te_2$ (3.82 g, 9.45 mmol) were loaded into a 250 mL three-neck round-bottom flask equipped with a magnetic stir bar, thermocouple, condenser, and vacuum adapter. The mixture was heated to 90 °C under Ar with continuous stirring to melt HDA and to homogenize the reagents. The low boiling liquids, such as possible water and acetic acid admixtures, were removed by degassing the mixture at 90 °C for 3 h. Then, the flask was rapidly heated to 300 °C under Ar and heated at this temperature for 1 h to react the Bi, Te, and Se precursors. Next, the resultant grey-black reaction mixture was cooled to 70 °C and diluted with 100 mL of toluene under stirring. After cooling to room temperature, the resultant NPs were precipitated by the addition of a solvent mixture consisting of toluene and ethanol (3 : 1) and collected by centrifugation at 9000 rpm for 5 min. The solid was washed twice with the same solvent mixture and again collected by centrifugation. After drying in vacuum, the NPs were homogenized using an agate mortar and pestle to provide as-synthesized optimally doped $Bi_2Te_{2.7}Se_{0.3}$ NPs (~4.6 g; ~92%) as powder.

### 2.3 Consolidation of $Bi_2Te_{2.7}Se_{0.3}$ particles into bulk material by SPS

$Bi_2Te_{2.7}Se_{0.3}$ NPs were compacted into macroscopic bulk pellets by employing rapid heating rates. The NPs were loaded on a graphite die having a single layer of graphite foil placed between the graphite plungers and the inner periphery of the die to prevent sample sticking onto the die during sintering. The sintering profile as shown in Fig. S1† comprises three continuous stages after vacuum $\approx$0.1 mbar is created in the chamber. In the first stage, both temperature and pressure were raised simultaneously up to 573 K and 50 MPa, respectively, before sintering. Subsequently, pressure was maintained and the temperature was gradually increased up to 623 K in the second stage and without holding, finally cooled to room-temperature in the third stage. The average ramp rates for heating and cooling were *ca.* 50 K $min^{-1}$ and 100 K $min^{-1}$, respectively. The previous reports on the correlation of sintering parameters (*i.e.*, peak temperature, holding time, and ramp rates) with transport properties were taken into account to determine the optimal sintering conditions that prevent grain growth and attain maximal density.[26,37,38] The pelletization was carried out by heating up to 623 K without any holding time and applying a uniaxial pressure of 50 MPa under a vacuum of $\approx$0.1 mbar to avoid oxidation. The relative density of the obtained disk-shaped pellet with dimensions of 12.7 mm × 2 mm was measured to be 95% using the Archimedes principle (822e Mettler Toledo).

### 2.4 Characterization

The morphology was studied by scanning electron microscopy (SEM) using a Helios NanoLab 450S DualBeam microscope

 

(FEI). The powder X-ray diffraction (XRD) patterns were collected using an X'Pert PRO diffractometer (PANalytical) set at 45 kV and 40 mA and equipped with $CuK_\alpha$ radiation and a PIXcel detector. The XRD patterns were matched to the International Centre for Diffraction Data database PDF-4+ (ICDD): 04-020-9373 using HighScore software package (PANalytical). High-angle annular dark-field scanning transmission electron microscopy (HAADF-STEM), selected-area electron diffraction (SAED), and energy-dispersive X-ray spectroscopy in STEM mode (STEM-EDX) were performed using a JEM-ARM200F cold FEG probe and image aberration corrected microscope, operated at 200 kV and equipped with a large-angle CENTURIO EDX detector.

### 2.5 Thermoelectric measurement

The measurements were performed in directions parallel (cross plane) and perpendicular (in-plane) to the pressing direction as shown in Fig. S2a.† All obtained values are the average of at least three replicates.

For thermal diffusivity ($D$) measurement, a circular disc specimen diameter of 12.7 mm, and thickness of 2 mm, as shown in Fig. S2b,† were used with a laser flash analyzer (LFA 1000, Linseis). Due to the disk-shaped sample requirement, the thermal diffusivity measurements were conducted only along the cross-plane direction. Simultaneously, specific heat measurements ($C_p$) were carried out using differential scanning calorimetry (DSC 404 F3 Pegasus, Netzsch). The rectangular bars with approximate dimensions of $10 \times 2 \times 2$ mm, as shown in Fig. S2c,† were cut from the bulk fabricated disc to prepare the specimens for electrical measurements along the cross-plane and in-plane directions. The four-probe DC method (ZEM-3, ULVAC-RIKO) was used to measure the $\sigma$ and $\alpha$ in a low-pressure He environment with temperatures ranging from 300 to 473 K. The room temperature Hall measurement was carried out with a magnetic field strength of 0.5 T, and the carrier concentration ($n$) and mobility ($\mu$) were calculated from the equations: $R_H = 1/ne$, and $\sigma = ne\mu$, where $e$ is the electrical charge of the electron. The observational error due to relative uncertainty in the transport properties measurement was $\pm 6\%$ for thermal diffusivity, $\pm 5\%$ for electrical conductivity, $\pm 5\%$ for Seebeck coefficient, $\pm 10\%$ for specific heat, and $\pm 1\%$ for density. The propagation of error due to instrumental precision in thermal conductivity, power factor, and $ZT$ is expressed in the graphs using error bars.

### 2.6 Computational details

We performed *ab initio* calculations for computing the electronic properties of the bulk $Bi_2Te_{2.7}Se_{0.3}$. The electronic structure was calculated using the Siesta DFT package.[39] The core electrons were modelled using norm-conserving fully-relativistic pseudopotentials from the PseudoDojo online database,[40] while valence electrons from s, p, and semi-core d orbitals were modelled using the TZP basis set during geometry optimization. For band structure calculations, basis sets were fitted to reproduce semiconductor band structures from more rigorous plane wave calculations.[41] The exchange and correlation terms were modelled using Perdew–Wang 91 functional[42] and the reciprocal space was sampled using Monkhorst–Pack grid up to $71 \times 71 \times 15$ $k$-points.[43] Spin–orbit coupling was modelled within on-site approximation of Ferrer.[44]

Electronic structure calculations were performed on a conventional unit cell of hexagonal crystalline lattice. The starting coordinates of atoms and lattice vectors were taken from experimental measurements for $Bi_2Te_{2.7}Se_{0.3}$.[45] Atomic positions were relaxed until forces per atom were below 0.01 eV $Å^{-1}$. Doping with Se was modelled within a virtual crystal approximation.[46] To implement it within Siesta, we placed virtual atoms, equivalent to a 9 : 1 Te/Se ratio, at all Te sites. The pseudopotential corresponding to the virtual atom was constructed by mixing pseudopotentials of Te and Se using the Mixps tool of Siesta distribution. To account for thermal expansion, electronic structure calculations were performed for a unit cell, and corrected using polynomial fits for expansion coefficients to experimental data for pure $Bi_2Te_3$ as a major component.[47]

TE transport coefficients were estimated within Boltzmann transport theory using the BoltzTraP2 package.[48] Constant relaxation time approximation was used to extract the following transport coefficients: $\alpha$ (Seebeck coefficient), $\sigma/\tau$ (normalized electric conductivity), and $\kappa_e/\tau$ (normalized electronic contribution to thermal conductivity). The average relaxation time $\tau =$ 8.4 fs was estimated by fitting the theoretical electric conductivity to the experimental measurements at 300 K.[30] This agrees well with the known relaxation time of 10 fs for bulk $Bi_2Te_3$.[49] The power law of electron–phonon relaxation time $\tau \sim T^{-3/2}$ was used to model its temperature dependence.[11]

For direct comparison of theoretical calculations with our experimental measurements we estimated transport coefficients at the values of chemical potential, corresponding to the desired temperature and the experimentally measured free carrier concentration. The calculated anisotropic transport coefficients were evaluated along the $c$-axis and along the $a$, $b$ axis to define the limits of the randomly oriented nanoparticles present in the experimental setup.

## 3. Results

### 3.1 Gram-scale route to hexagonal-shaped plate-like $Bi_2Te_{2.7}Se_{0.3}$ particles

We adapted our recently developed colloidal synthesis route[36] for the preparation of a targeted $Bi_2Te_{2.7}Se_{0.3}$ compound *via* reacting $Bi(ac)_3$ with $Ph_2Se_2/Ph_2Te_2$ in a fatty amine solvent at 300 °C. To account for the volatile nature and high vapour pressure of chalcogenides (Te/Se),[13] we used a 10 mol% excess of $Ph_2Se/Ph_2Te_2$ in our protocol. Since the initial synthesis attempts to prepare 1 g of $Bi_2Te_{2.7}Se_{0.3}$ were successful, we scaled up the synthesis to provide ≈4.6 g of $Bi_2Te_{2.7}Se_{0.3}$ with a yield of ≈92% in a reproducible manner.

According to the XRD analysis (Fig. 1a), the as-synthesized product is a phase-pure material crystallized in the rhombohedral crystal system [space group $R\bar{3}m$ (no. 166)]. Using Rietveld refinement, the unit cell parameters were estimated to be

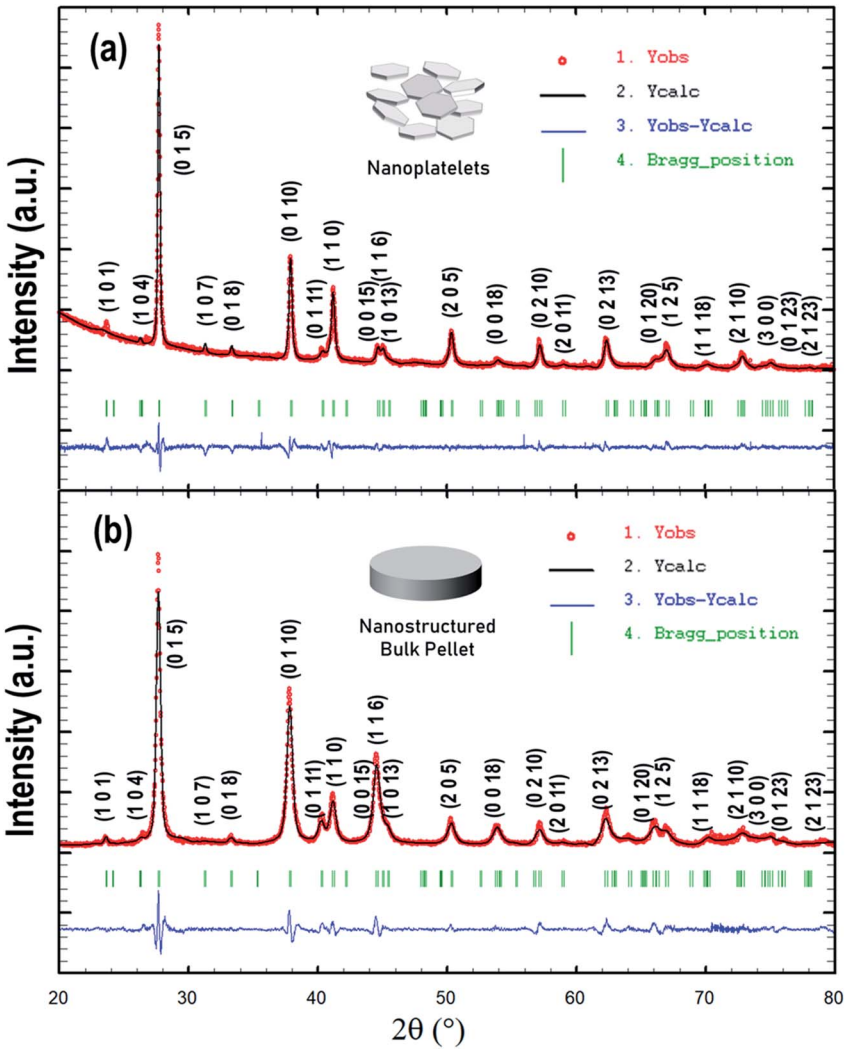


Fig. 1 Results of Rietveld refinement of experimental X-ray diffraction patterns for $Bi_2Te_{2.7}Se_{0.3}$ (a) as-synthesized nanocrystals and (b) bulk sintered nanostructured sample.

$a = b = 4.381$ Å, $c = 30.415$ Å, $\alpha = \beta = 90°$, and $\gamma = 120°$ (Table 1), which are consistent with previous reports.[45] SEM imaging of the product shows a plate-like appearance of the resultant $Bi_2Te_{2.7}Se_{0.3}$ particles, predominantly featuring hexagonal shapes. The particles exhibit a quite broad size distribution with the length in the sub-micron/micron-size regime and thickness of about several tens of nanometres, *i.e.*, a few quintuple layers (Fig. 2a). HAADF-STEM observation at low-magnification further verified the hexagonal-shaped plate-like morphology, while the respective STEM-EDX mapping revealed the homogeneous distribution of the Bi, Te, and Se elements in the synthesized particles (Fig. 2b). EDX analysis also shows that the average chemical composition of the particles is $Bi_2Te_{2.74}Se_{0.26}$, with slightly depleted Se content *versus* the desired $Bi_2Te_{2.7}Se_{0.3}$ compositions.

To gain information about the fine microstructure and the structural arrangement in $Bi_2Te_{2.7}Se_{0.3}$ particles synthesized by colloidal synthesis, we further conducted a HAADF-STEM study in conjunction with SAED analysis. Fig. 3 shows representative high-resolution HAADF-STEM images of the as-synthesized

Table 1 Rietveld refinement parameters of the synthesized $Bi_2Te_{2.7}Se_{0.3}$ nanoplatelets and bulk nanostructured alloys

| | $R_p$ | $R_{wp}$ | $R_e$ | $\chi^2$ | Cell parameters | $D_{avg}$ (nm) |
|---|---|---|---|---|---|---|
| $Bi_2Te_{2.7}Se_{0.3}$ nanocrystals | 41.0 | 22.9 | 11.10 | 4.24 | $a = b = 4.381$ Å, $c = 30.415$ Å<br>$\alpha = \beta = 90°$, $\gamma = 120°$ | 20 |
| BTS n-type | 14.2 | 16.1 | 8.97 | 3.21 | $a = b = 4.385$ Å, $c = 30.509$ Å<br>$\alpha = \beta = 90°$, $\gamma = 120°$ | 24 |

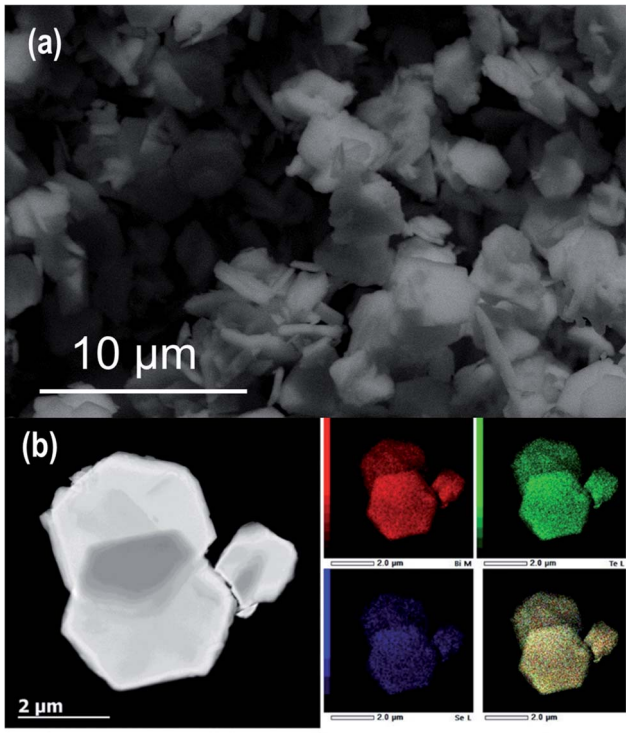


Fig. 2 Microstructural characterization of $Bi_2Te_{2.7}Se_{0.3}$ nanocrystals: (a) FE-SEM images; (b) HAADF-STEM image and the corresponding EDX elemental mapping of Bi M, Te L, Se L and overlaid color image.

plate-like particle along the [001] and [210] zone axes, together with the respective SAED patterns. One can observe that the sample is highly crystalline and remarkably defect free. The SAED patterns can be completely indexed in the rhombohedral crystal structure using unit cell parameters estimated by Rietveld refinement (Table 1). The overlaid structural models in high-resolution images agree well with experimental observation (Fig. 3), demonstrating the perfect structural arrangement in the resultant hexagonal-shaped plate-like $Bi_2Te_{2.7}Se_{0.3}$ particles.

### 3.2 Dense $Bi_2Te_{2.7}Se_{0.3}$ material formed from plate-like particles by SPS

Having in hand a large quantity of highly crystalline $Bi_2Te_{2.7}Se_{0.3}$ plate-like particles, we next used them to fabricate a bulk TE material *via* SPS employing rapid heating rates. During the SPS cycle, the passage of high current through powder produces localized heating within the grain boundaries, thereby limiting the grain growth and eliminating porosity. According to the XRD analysis (Fig. 1b), the as-sintered $Bi_2Te_{2.7}Se_{0.3}$ pellet (hereafter referred to as BTS) is a phase-pure material with refined rhombohedral unit cell parameters $a = b = 4.385$ Å, $c = 30.509$ Å, $\alpha = \beta = 90°$, and $\gamma = 120°$, which are quite similar to those of the initial plate-like particles above. The average crystallite sizes of the chemically synthesized $Bi_2Te_{2.7}Se_{0.3}$ particles ($\approx$20 nm) and sintered BTS samples ($\approx$24 nm), quantitatively assessed using XRD data employing the Williamson–Hall method (Table 1), indicate that nominal growth occurred during sintering. The relative density of the obtained disk-shaped pellet was measured to be $\approx$95%, which is close to the theoretical density. Such a high value may be attributed to an increased interface density within the densely packed microstructure by deterrent grain growth and densification at very fast heating and cooling rates.

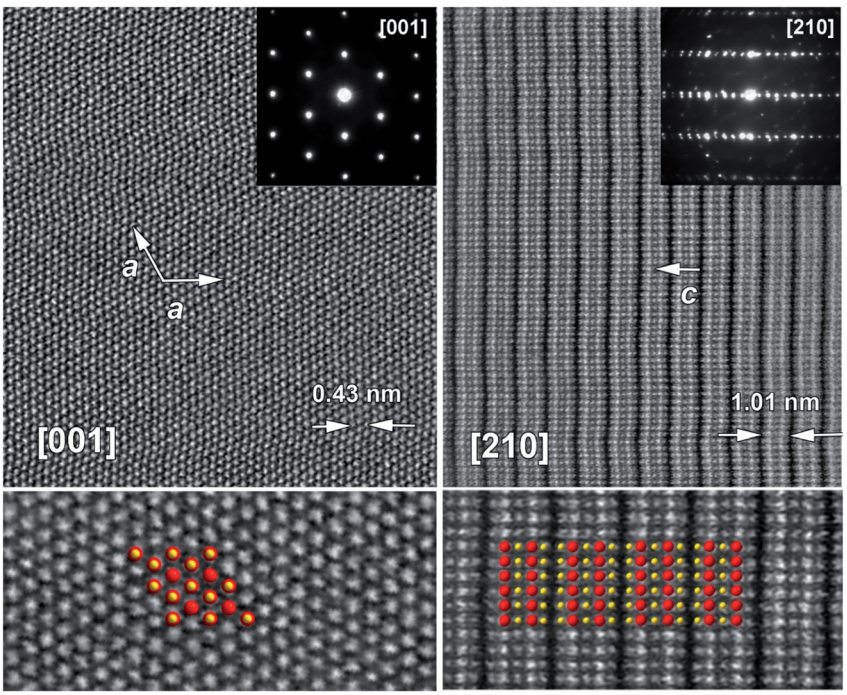


Fig. 3 HAADF-STEM characterization of $Bi_2Te_{2.7}Se_{0.3}$ nanocrystals for [001] and [210] zones together with enlargement images and structural model overlay (Bi: red, Te/Se: yellow). Insets show corresponding SAED diffraction patterns.

### 3.3 Nearly isotropic electrical transport in bulk nanostructured n-type BTS

Next, we aimed to understand the transport properties of the resultant SPS-sintered BTS materials. Despite the wide range of studies on BTS systems, it is not straightforward to directly compare the transport characteristics between the bulk crystalline material and nanostructured samples. The reason for this is that substantial doping of $Bi_2Te_3$-based materials results in lattice defects,[50–52] which affect the free carrier density and, therefore, transport properties over a wide range.[53–55] The reported electric conductivity changes from $\sim 0.2–0.4 \times 10^5$ S m$^{-1}$ for macroscale crystalline ingots[56,57] and up to $\sim 1.0 \times 10^5$ S m$^{-1}$ for nanostructured samples.[30] This is attributed to a higher concentration of defects in the nanostructured material especially at nanoparticle interfaces. Therefore, it is more insightful to compare experimental measurements with the theoretically calculated properties, estimated at the value of chemical potential yielding the same free carrier concentration measured in a particular experiment. This way the effect of different defect concentrations due to different fabrication methods is avoided.

Experimentally, the anisotropy in the electrical transport between the *ab*-plane and the *c*-axis of single crystalline $Bi_2Te_3$ alloys has been widely recognized especially in ingots made by unidirectional crystal growing methods.[31,58] Also, $Bi_2Te_3$ and its alloys were found to be susceptible to deformation-induced defects, which affects the electrical transport properties.[16,19,30] Hence, in the BTS fabricated from plate-like particles, the temperature dependent anisotropy of the electrical transport properties of bulk BTS samples were examined in both the in-plane and cross-plane direction for three subsequent runs, as shown in ESI Fig. S3.† Each measurement scan was carried out only in a heating mode from room temperature to 473 K, which took approx. 2 hours to complete.

The temperature dependent $\sigma$ shown in Fig. S3(a)† along both directions exhibits degenerate semiconducting behavior and is higher at lower temperature for the in-plane direction. This is similar to observations made previously for crystallographically textured n-type $Bi_2Te_{3-x}Se_x$ and can be ascribed to higher charge carrier mobility along the (*a*, *b*) crystal plane than in the *c* direction.[16] The temperature dependent $\alpha$ as shown in Fig. S3(b)† increases with increasing temperature and exhibits negative values of $\alpha$, for measurements along both directions. The measured $\alpha$ vary marginally for lower temperatures and exhibit higher values along the cross-plane direction. However, at higher temperature, the variation becomes more distinct and can be ascribed to the intrinsic excitation of minority charge carriers, which likewise is stabilized for successive measurement runs.

The anisotropic difference observed in as-synthesized sintered BTS alloys along both in-plane and cross-plane measurements for $\sigma$ were significantly reduced and for $\alpha$ is distinctively evident after the initial measurement run that can be attributed to partial annealing that occurs at higher temperature measurements, which subsequently relieves the thermal stress and alleviates lattice defects arisen during rapid sintering. These observations are in line with the previously observed annealing effects on the electrical properties of n-type $Bi_2Te_3$ for annealing done at 423 K.[59] The measured $\sigma$ and $\alpha$ remain unaffected over temperature excursions for successive runs in the measured temperature range. The thermally stabilized synthesized BTS were found to exhibit weakened anisotropy as observed previously for nanostructured bulk polycrystalline n-type $Bi_2Te_{3-x}Se_x$.[15,30]

Due to the disk-shaped sample requirement for thermal diffusivity measurement as shown in Fig. S2(b),† the measurement for thermal transport was done only along the cross-plane direction. Notably, both electrical and thermal characterization in the cross-plane direction for the thermally stabilized sample were analysed and are presented in the subsequent section to marginalise the effect of non-homogeneity and crystallographic orientations introduced during sintering, thus minimizing the possibility of erroneous data.

### 3.4 Low effective mass and high carrier mobility in n-type BTS

The experimental measurements and theoretical estimations of the temperature-dependent TE transport property of the resultant bulk nanostructured BTS sample are shown in Fig. 4. We first investigated the electrical transport of BTS. The $\sigma$ displayed in Fig. 4a slightly decreases with increasing temperature, indicating a degenerate semiconducting behaviour. The experimental $\sigma$ lies between the theoretical estimates for BTS as

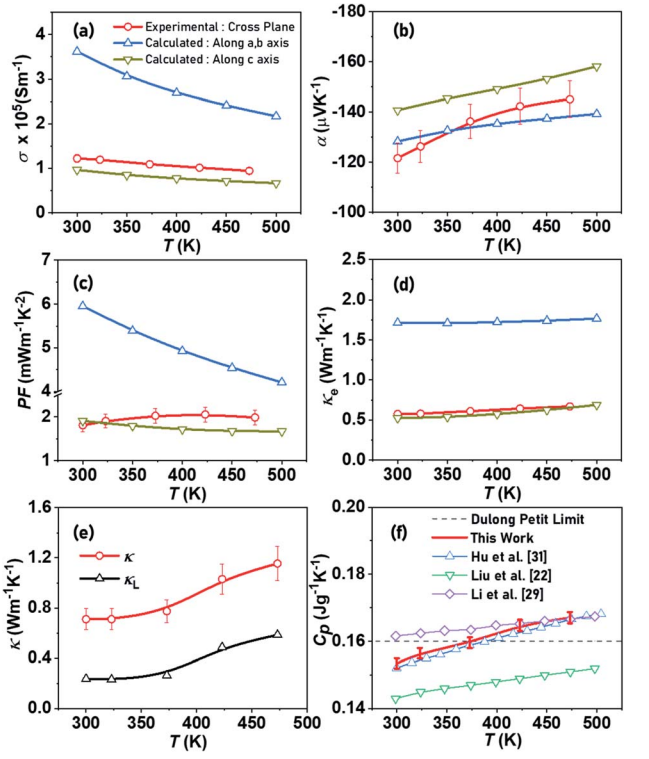


Fig. 4 Temperature-dependent transport properties of synthesized $Bi_2Te_{2.7}Se_{0.3}$ nanostructured bulk alloy, BTS (a) electrical conductivity, (b) Seebeck coefficient, (c) power factor, (d) electronic thermal conductivity, (e) total and lattice thermal conductivity, and (f) specific heat capacity.[22,29,31]

a result of optimal carrier concentration $n \approx 2.5 \pm 0.5 \times 10^{19}$ $cm^{-3}$ and high carrier mobility $\mu \approx 240 \pm 5$ $cm^2 V^{-1} s^{-1}$, which is comparable to previous reports.[20,26,60] The theoretical dependence of $\sigma$ is the result of competing processes of a growing number of charge carriers along with a rapidly decaying electron–phonon relaxation time (Fig. 4a).

The plot of $\alpha$ is depicted in Fig. 4b, which exhibits negative values ranging from $-120$ to $-145$ $\mu V K^{-1}$, indicating that n-type conduction occurs with electrons as the majority charge carriers. It can be observed that $\alpha$ increases with increasing temperature both experimentally and theoretically, which can be associated to the solubility of Se (at Te sites) in $Bi_2Te_3$ that creates donor levels in the band gap of $Bi_2Te_3$, leading to favourable modification in the electronic density of states (DOS). This inhibits the onset of intrinsic minority carrier conduction in the synthesized BTS at higher temperature, which is in line with the theoretical estimates predicting an increase in $\alpha$ with temperature and within the similar range. The increasing $\alpha(T)$ estimated theoretically accounts for a considerable presence of minority charge carriers in the measured temperature range due to the narrow band gap of $Bi_2Te_3$.[6] The growth of $\alpha$ measured in this work reflects the strong effect of nanostructuring and band-gap engineering on electronic properties in suppressing the bipolar transport within the measured temperature regime.

To further elucidate the degenerate electrical transport of the synthesized BTS, we estimated the carrier effective mass ($m^*$) based on the energy-independent relaxation time approximation using the Pisarenko relationship between $\alpha$ and $n$, which is expressed as $\alpha = (8\pi^2 k_B^2/3eh^2)m^*T(\pi/3n)^{2/3}$, wherein $k_B$ and $h$ are the Boltzmann constant and Planck constant, respectively. Assuming a single parabolic band, $\alpha$ at any given temperature can be described by a unique value of $m^*$. This value for the SPS-sintered BTS at room temperature was calculated to be $0.52m_e$, where $m_e$ represents the mass of an electron. Thus, the low $m^*$ explains the high $\mu$ and lower values of $\alpha$ attained in the prepared BTS material. The cumulative measurement of electrical transport, *i.e.*, power factor (PF, $\alpha^2\sigma$), revealed a high value, which decreases with increasing temperature (Fig. 4c). The PF lies in the range of 1.8–2.1 mW $m^{-1}$ $K^{-2}$, which is closer to theoretical estimates along the $c$ axis and is comparable to previous reports on similar compositions.[15–22,29–32] Moreover, on average the experimentally attained PF is higher than the theoretical estimates (along the same axis), which may be ascribed to suppressed bipolar conduction, low $m^*$, and high $\mu$.

### 3.5 Reduced thermal conductivity in BTS due to grain boundary scattering

The electronic thermal conductivity (Fig. 4d) can be experimentally evaluated according to the Wiedemann–Franz law $\kappa_e = L \times \sigma \times T$, where $L$ is the Seebeck-dependent Lorenz number.[61] The $L$ values are in the range of $(1.7–1.8) \times 10^{-8}$ W Ω $K^{-2}$. Similar to theoretical estimates, the experimental $\kappa_e$ varies marginally in the measured temperature regimes and is in close agreement with estimates along the $c$-axis as anticipated for cross-plane measurements. It is evident that the experimentally measured $\sigma$ and the $\kappa_e$ closely follow the theoretical estimates for a macroscale BTS crystal in the direction of the $c$-axis of the hexagonal lattice, *i.e.* perpendicular to the plane of easy cleavage and, hence, larger contact area. This is an intriguing observation as it shows that the samples prepared in this work sustain bulk-like electric conductivity, while suppressing lattice thermal conduction.

After revealing the electrical transport characteristics of BTS, we then moved forward with probing thermal transport in the TE material. The total thermal conductivity was calculated using the equation $\kappa = D \times \rho \times C_p$. As shown in Fig. 4e, $\kappa$ is significantly suppressed at lower temperature, which may be ascribed largely to grain boundary scattering by nanostructuring. However, with rising temperature, $\kappa$ increases due to intrinsic excitation, resulting in the ambipolar diffusion of electron–hole pairs. A minimal $\kappa \approx 0.7$ W $m^{-1}$ $K^{-1}$ at 300 K is attained, which is among the lowest reported[15–22,29–32] in a polycrystalline n-type $Bi_2Te_3$-based composition and can mainly be attributed to the plate-like microstructural features of the constituting particles (Fig. 2).[62] The lattice thermal conductivity was calculated using the equation $\kappa_L = \kappa - \kappa_e$ and is presented along with $\kappa$ in Fig. 4e. The $\kappa_L$ is significantly suppressed at lower temperature, which can be attributed to grain boundary scattering resulting from bulk nanostructuring in the SPS-sintered BTS.[63] The nanosized features specifically target the scattering of low frequency phonons with a long mean free path, as observed in the synthesized bulk nanostructured BTS.

Additionally, alloy scattering supplemented by mass fluctuation due to isoelectronic Se substitution synergistically contribute towards the enhancement of phonon scattering.[64] Further reduction in the $\kappa_L$ of the synthesized BTS can be achieved using nano-microstructural alteration, doping and disordering by high pressure and high strain deformation.[63–65] In the $\kappa$ estimation particularly at higher temperatures, the uncertainty in the absolute magnitude of $C_p$ measurements of systems, especially those having substantial latent heats (*e.g.*, during phase transitions), often leads to inaccuracy in calculating their $\kappa$ (≈10% or more).[66] Generally, the temperature-independent Dulong–Petit heat capacity provides a close approximation near room temperature, which can be modeled at higher temperatures assuming linear temperature dependence. The temperature-dependent $C_p$ measurement of the synthesized nanostructured BTS sample shown in Fig. 4f is found to be in close proximity to the Dulong–Petit limit and in a similar range as reported previously.[22,29,31]

### 3.6 High thermoelectric $ZT_{avg} \approx 0.93$ over 300–473 K range

Fig. 5a shows the $ZT$ values as a function of temperature for the SPS-sintered n-type BTS. The material exhibits high $ZT$ near lower temperatures with a $ZT_{max} \approx 1$ at 373 K for the cross-plane direction, which is comparable to the highest $ZT$ in n-type $Bi_2Te_3$-based TE materials.[15–22,29–32] The low effective mass, high carrier mobility, and relatively low $\kappa_L$ boost the TE performance of the as-synthesized n-type $Bi_2Te_{2.7}Se_{0.3}$ alloy to the state-of-the-art level. Furthermore, the $ZT_{avg}$ in the measured temperature range is evaluated using[67]

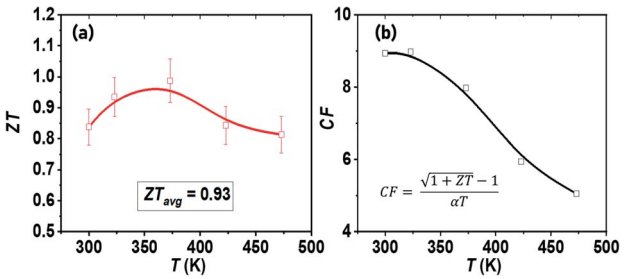


Fig. 5 Temperature-dependent (a) thermoelectric figure of merit ($ZT$) and (b) thermoelectric compatibility factor (CF), of synthesized $Bi_2Te_{2.7}Se_{0.3}$ bulk nanostructured alloys.

$$ZT_{avg} = \frac{1}{T_h - T_c}\int_{T_c}^{T_h} ZT\,dT$$

The observed excellent average $ZT_{avg} \approx 0.93$ in the low temperature range *i.e.* 300–473 K is attributed to the synergistic combination of reduced $\kappa_L$ and maintained high power factor in the measured temperature range.

In support of the fact that our BTS is a good TE material, we further considered its compatibility factor, which is an important characteristic for real TE device application. Even in the case of high temperature sources, the thermoelements can be segmented by using $Bi_2Te_3$-based materials at low temperature ends, since they are the best available TE materials for low temperature applications.[6] The efficacy of such segmentation is calculated by the TE compatibility factor[68] $CF = \frac{\sqrt{1+ZT}-1}{\alpha T}$. The CF of the SPS-sintered n-type BTS nanostructured alloys is shown in Fig. 5b. From an applicability perspective in segmentation, the difference in CF for the two TE materials should be less than a factor of 2. The calculated CF of our TE material decreases with increasing temperature as a result of its direct correlation with $ZT$, and it is comparable to other state-of-the-art n-type TE materials in the mid-temperature range.[69] This result suggests that n-type BTS formed from plate-like particles will also be a suitable TE material for segmentation with high-performance mid-temperature TE materials,[22] such as PbTe[70] and half-Heuslers,[71–74] for achieving efficient TE energy conversion.

# 4. Discussion

## 4.1 Correlation of chemical synthesis with high TE performance

The scalable synthesis of phase pure and highly crystalline nanomaterials with homogeneous and controllable chemical composition, size, and shape is a pre-requisite to commercialize the newly developed approaches to production levels. Traditionally, $Bi_2Te_3$-based alloys were mainly synthesized employing high-temperature alloying, wherein high purity elemental precursors are co-melted at temperatures above 773 K, and kept for a prolonged period of time at such elevated temperature for homogeneous mixing, followed by gradual cooling. For large-scale commercial applications, zone melting is a commonly used production technology for $Bi_2Te_3$-based materials and devices.[31] Despite higher power factors achieved in several studies, a proportional increase in $\kappa$ due to coupling had largely limited efforts aimed towards $ZT$ enhancement.[6,16,29,30] Although orienting crystallographic planes by texturing[16,75] and deformation[31,32,76] were found effective to achieve higher $ZT$, the anisotropic trends of TE transport due to deformation-induced defects are not well established as higher $ZT$ were achieved both in planes parallel[16] and perpendicular[30] to the pressing direction.

The nanostructuring approaches for $\kappa$ reduction by random grain orientations and grain size reduction often tend to impede the carrier transport, thereby deteriorating $\mu$ in nanocrystalline materials. In principle, $ZT$ could be greatly improved if nanostructured grains were preferentially oriented to achieve $\kappa$ reduction while maintaining the high power factor. Herein, a novel large-scale chemical alloying synthesis that allows precise substitutional doping has been demonstrated for the synthesis of a bulk nanostructured BTS alloy at a much lower temperature and energy requirement than traditionally used energy-intensive processes such as ball milling[20–22,28–30] and melt-spinning.[19,27,33,34] This approach combines a colloidal synthesis method and thermal SPS processing under controlled heating conditions under inert atmosphere. Moreover, the uniaxial pressure and optimal sintering conditions assist the favorable orientation of particle domains with limited grain growth. We show that this preparation approach allows the realization of a *ca.* 5 g batch of $Bi_2Te_3$ and its derivatives with nearly stoichiometric chemical doping.

It is widely acknowledged that different synthesis methodology results in distinct physical and transport properties, highlighting the vital role of material processing. The nanostructuring routes that were implemented for bulk TEs mainly comprise two steps: (i) producing nanostructured powders and (ii) their consolidation into bulk by sintering. A comparison of the presented methodology with nanostructuring approaches, such as solvothermal,[15] hydrothermal,[18] melt-spinning,[19] and ball milling,[20,30] in the recent literature for pristine $Bi_2Te_{2.7}Se_{0.3}$ bulk nanostructured alloys is summarized in Fig. 6. This comparison suggests that the attained $ZT$ in the measured

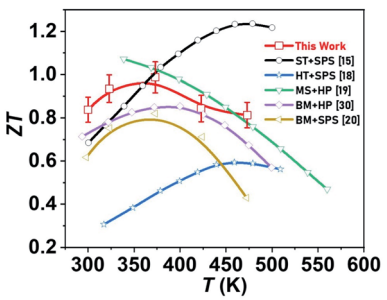


Fig. 6 $ZT$ comparison with state-of-the-art of $Bi_2Te_{2.7}Se_{0.3}$ nanostructured bulk alloys synthesized by solvothermal (ST),[15] hydrothermal (HT),[18] melt-spinning (MS),[19] ball-milling (BM),[20,30] consolidated employing hot pressing (HP)[19,30] and spark plasma sintering (SPS).[15,18,20]

temperature range is comparable to those obtained through other nanostructuring routes, and can also give rise to the scalable synthesis of high-performance $Bi_2Te_3$-based TE materials. Further *ZT* enhancement is achievable in the synthesized bulk nanostructured BTS by applying hot deformation,[31,32,76] liquid state manipulation,[16,75] doping (*via* Cu,[52] K,[77] and I[78] dopants), and nanocomposite (using $SnS_2$,[79] GaAs,[80] and InSb[29] nanoparticles) approaches.

### 4.2 High *ZT* from high carrier mobility and low frequency phonon scattering

The BTS alloy prepared from the high quality $Bi_2Te_{2.7}Se_{0.3}$ plate-like particles is a solid solution of bismuth telluride with the isomorphous bismuth selenide, which displays high $\mu$ with optimal $n$ and reduced $\kappa_L$. Thus, the nanostructure-induced enhanced scattering of phonons in this solid solution does not reduce the $\mu$ resulting in high PF and low $\kappa$, which synergistically led to favourable thermal and electrical transport for achieving high *ZT*. The experimentally measured electrical properties exhibit inverse correlation with $\alpha$ and $\sigma$ with n-type degenerate semiconducting charge transport, in close agreement to the theoretically estimated mixed conduction. The suppressed bipolar conduction and shifting of thermal excitation of minority charge carriers to higher temperature resulted in improved electrical transport that corroborated the theoretical estimates, which does not account for nanostructuring.

The ultra-low $\kappa_L$ attained in the BTS alloy was mainly attributed to the enhanced grain boundary scattering of low frequency phonons (dominant in near room temperature regimes) by arrays of dislocations at semi-coherent grain boundaries and micro-, sub-micro-, and nano-scale domains in the lattice structure (Fig. 2). Such a microstructure will allow selective scattering of only phonons and will not impact electrons/holes, which have relatively longer wavelengths as indicated by higher $\mu$, thus attaining higher $\sigma$ (Fig. 4a). Our current data indicate that a combination of large-scale colloidal synthesis of $Bi_2Te_{2.7}Se_{0.3}$ plate-like particles with judicious spark plasma sintering is critical for achieving high $ZT_{max} \approx 1$ (373 K) and remarkable $ZT_{avg} \approx 0.93$ (300–473 K). Importantly, these values are among the highest reported for n-type $Bi_2Te_3$-based TE alloys.[15–22,29–32]

## 5. Conclusion

In summary, we have reported the large-scale colloidal synthesis of hexagonal-shaped plate-like $Bi_2Te_{2.7}Se_{0.3}$ particles. Their detailed characterization revealed the phase purity, high crystallinity, and chemical uniformity of the as-synthesized material. The $Bi_2Te_{2.7}Se_{0.3}$ particles were consolidated into a dense bulk material by time-efficient spark plasma sintering and the resultant n-type thermally stabilized $Bi_2Te_{2.7}Se_{0.3}$ alloy demonstrates high room temperature carrier mobility of *ca.* 240 $cm^2\ V^{-1}\ s^{-1}$ at an optimal carrier concentration of *ca.* $2.5 \times 10^{19}\ cm^{-3}$, achieving a higher average power factor of $\approx 2$ mW $m^{-1}\ K^{-2}$. The micro-, sub-micro-, and nano-scale features of constituent $Bi_2Te_{2.7}Se_{0.3}$ particles were reflected in the ultra-low room temperature total thermal conductivity of *ca.* 0.7 W $m^{-1}\ K^{-1}$ in the sintered material. Thereby, the as-prepared $Bi_2Te_{2.7}Se_{0.3}$ alloy delivers a high figure of merit $ZT \approx 1$ at 373 K with average $ZT \approx 0.93$ (300–473 K). The potential of bulk nanostructuring in $Bi_2Te_{2.7}Se_{0.3}$ alloys is corroborated by comparing the experimental outcomes of TE transport with theoretical estimates obtained by *ab initio* modeling. The enhancement in *ZT* is primarily ascribed to suppressed bipolar conduction leading to a higher power factor with a simultaneous reduction in lattice thermal conductivity due to the significant grain boundary scattering by bulk nanostructuring.

## Data availability statement

The data that support the findings of this study are available upon request from the authors.

## Conflicts of interest

There is no conflict of interest to declare.

## Acknowledgements

We thank the members of the Nanochemistry Research Group (http://nanochemgroup.org) at INL for insightful discussions and support. This work was supported by Portuguese National Funding Agency for Science, Research and Technology (FCT) under the UT-BORN-PT project (UTAP-EXPL/CTE/0050/2017). B. A. K. acknowledges funding of this work by the Robert A. Welch Foundation (grant no. F-1464). The authors acknowledge the Texas Advanced Computing Center (TACC) at The University of Texas at Austin for providing HPC resources that have contributed to the research results reported within this paper. URL: http://www.tacc.utexas.edu.

## References

1 R. Freer and A. V. Powell, *J. Mater. Chem. C*, 2020, **8**, 441–463.
2 F. J. DiSalvo, *Science*, 1999, **285**, 703–706.
3 G. Snyder and E. Toberer, *Nat. Mater.*, 2008, **7**, 105–114.
4 D. Beretta, N. Neophytou, J. M. Hodges, M. G. Kanatzidis, D. Narducci, M. Martin-Gonzalez, M. Beekman, B. Balke, G. Cerretti and W. Tremel, *Mater. Sci. Eng., R*, 2019, **138**, 100501.
5 D. Wright, *Nature*, 1958, **181**, 834.
6 H. J. Goldsmid, *Materials*, 2014, **7**, 2577–2592.
7 I. Petsagkourakis, K. Tybrandt, X. Crispin, I. Ohkubo, N. Satoh and T. Mori, *Sci. Technol. Adv. Mater.*, 2018, **19**, 836–862.
8 C. Dagdeviren, Z. Li and Z. L. Wang, *Annu. Rev. Biomed. Eng.*, 2017, **19**, 85–108.
9 N. Nandihalli, C.-J. Liu and T. Mori, *Nano Energy*, 2020, **78**, 105186.
10 Z. Soleimani, S. Zoras, B. Ceranic, S. Shahzad and Y. Cui, *Sustainable Energy Technologies and Assessments*, 2020, **37**, 100604.

11 I. T. Witting, T. C. Chasapis, F. Ricci, M. Peters, N. A. Heinz, G. Hautier and G. J. Snyder, *Adv. Electron. Mater.*, 2019, **5**, 1800904.
12 J. P. Heremans, R. J. Cava and N. Samarth, *Nat. Rev. Mater.*, 2017, **2**, 1–21.
13 Y. Liu, Y. Zhang, S. Ortega, M. Ibáñez, K. H. Lim, A. Grau-Carbonell, S. Martí-Sánchez, K. M. Ng, J. Arbiol and M. V. Kovalenko, *Nano Lett.*, 2018, **18**, 2557–2563.
14 M. Scheele, N. Oeschler, I. Veremchuk, K.-G. Reinsberg, A.-M. Kreuziger, A. Kornowski, J. Broekaert, C. Klinke and H. Weller, *ACS Nano*, 2010, **4**, 4283–4291.
15 M. Hong, T. C. Chasapis, Z.-G. Chen, L. Yang, M. G. Kanatzidis, G. J. Snyder and J. Zou, *ACS Nano*, 2016, **10**, 4719–4727.
16 Y. Liu, Y. Zhang, K. H. Lim, M. Ibáñez, S. Ortega, M. Li, J. David, S. Martí-Sánchez, K. M. Ng and J. Arbiol, *ACS Nano*, 2018, **12**, 7174–7184.
17 A. Soni, Z. Yanyuan, Y. Ligen, M. K. K. Aik, M. S. Dresselhaus and Q. Xiong, *Nano Lett.*, 2012, **12**, 1203–1209.
18 D. Li, X. Qin, Y. Dou, X. Li, R. Sun, Q. Wang, L. Li, H. Xin, N. Wang and N. Wang, *Scr. Mater.*, 2012, **67**, 161–164.
19 O. Meroz, N. Elkabets and Y. Gelbstein, *ACS Appl. Energy Mater.*, 2020, **3**, 2090–2095.
20 S. T. Han, P. Rimal, C. H. Lee, H.-S. Kim, Y. Sohn and S.-J. Hong, *Intermetallics*, 2016, **78**, 42–49.
21 Y. Pan, T.-R. Wei, C.-F. Wu and J.-F. Li, *J. Mater. Chem. C*, 2015, **3**, 10583–10589.
22 W. Liu, K. C. Lukas, K. McEnaney, S. Lee, Q. Zhang, C. P. Opeil, G. Chen and Z. Ren, *Energy Environ. Sci.*, 2013, **6**, 552–560.
23 L. Hicks and M. S. Dresselhaus, *Phys. Rev. B: Condens. Matter Mater. Phys.*, 1993, **47**, 12727.
24 V. Akshay, M. Suneesh and M. Vasundhara, *Inorg. Chem.*, 2017, **56**, 6264–6274.
25 V. Stavila, D. Robinson, M. Hekmaty, R. Nishimoto, D. Medlin, S. Zhu, T. Tritt and P. Sharma, *ACS Appl. Mater. Interfaces*, 2013, **5**, 6678–6686.
26 J. S. Son, M. K. Choi, M.-K. Han, K. Park, J.-Y. Kim, S. J. Lim, M. Oh, Y. Kuk, C. Park and S.-J. Kim, *Nano Lett.*, 2012, **12**, 640–647.
27 S. I. Kim, K. H. Lee, H. A. Mun, H. S. Kim, S. W. Hwang, J. W. Roh, D. J. Yang, W. H. Shin, X. S. Li and Y. H. Lee, *Science*, 2015, **348**, 109–114.
28 B. Poudel, Q. Hao, Y. Ma, Y. Lan, A. Minnich, B. Yu, X. Yan, D. Wang, A. Muto and D. Vashaee, *Science*, 2008, **320**, 634–638.
29 D. Li, J. Li, J. Li, Y. Wang, J. Zhang, X. Qin, Y. Cao, Y. Li and G. Tang, *J. Mater. Chem. A*, 2018, **6**, 9642–9649.
30 X. Yan, B. Poudel, Y. Ma, W. Liu, G. Joshi, H. Wang, Y. Lan, D. Wang, G. Chen and Z. Ren, *Nano Lett.*, 2010, **10**, 3373–3378.
31 L. Hu, H. Wu, T. Zhu, C. Fu, J. He, P. Ying and X. Zhao, *Adv. Energy Mater.*, 2015, **5**, 1500411.
32 L. Hu, T. Zhu, X. Liu and X. Zhao, *Adv. Funct. Mater.*, 2014, **24**, 5211–5218.
33 Y. Pan, U. Aydemir, J. A. Grovogui, I. T. Witting, R. Hanus, Y. Xu, J. Wu, C. F. Wu, F. H. Sun and H. L. Zhuang, *Adv. Mater.*, 2018, **30**, 1802016.
34 X. Tang, W. Xie, H. Li, W. Zhao, Q. Zhang and M. Niino, *Appl. Phys. Lett.*, 2007, **90**, 012102.
35 Z.-Y. Hu, Z.-H. Zhang, X.-W. Cheng, F.-C. Wang, Y.-F. Zhang and S.-L. Li, *Mater. Des.*, 2020, **191**, 108662.
36 V. Sousa, B. F. Gonçalves, M. Franco, Y. Ziouani, N. González-Ballesteros, M. Fátima Cerqueira, V. Yannello, K. Kovnir, O. I. Lebedev and Y. V. Kolen'ko, *Chem. Mater.*, 2018, **31**, 260–267.
37 L. Han, S. H. Spangsdorf, N. Nong, L. Hung, Y. Zhang, H. N. Pham, Y. Chen, A. Roch, L. Stepien and N. Pryds, *RSC Adv.*, 2016, **6**, 59565–59573.
38 M. Saleemi, M. S. Toprak, S. Li, M. Johnsson and M. Muhammed, *J. Mater. Chem.*, 2012, **22**, 725–730.
39 J. M. Soler, E. Artacho, J. D. Gale, A. García, J. Junquera, P. Ordejón and D. Sánchez-Portal, *J. Phys.: Condens. Matter*, 2002, **14**, 2745.
40 M. Van Setten, M. Giantomassi, E. Bousquet, M. J. Verstraete, D. R. Hamann, X. Gonze and G.-M. Rignanese, *Comput. Phys. Commun.*, 2018, **226**, 39–54.
41 P. Rivero, V. M. García-Suárez, D. Pereñiguez, K. Utt, Y. Yang, L. Bellaiche, K. Park, J. Ferrer and S. Barraza-Lopez, *Comput. Mater. Sci.*, 2015, **98**, 372–389.
42 C. Filippi, C. Umrigar and M. Taut, *J. Chem. Phys.*, 1994, **100**, 1290–1296.
43 H. J. Monkhorst and J. D. Pack, *Phys. Rev. B: Solid State*, 1976, **13**, 5188.
44 L. Fernández-Seivane and J. Ferrer, *Phys. Rev. Lett.*, 2007, **99**, 183401.
45 J. Dumas, G. Brun, B. Liautard, J. Tedenac and M. Maurin, *Thermochim. Acta*, 1987, **122**, 135–141.
46 R. Poloni, J. Iniguez, A. García and E. Canadell, *J. Phys.: Condens. Matter*, 2010, **22**, 415401.
47 L. M. Pavlova, Y. I. Shtern and R. E. e. Mironov, *High Temp.*, 2011, **49**, 369–379.
48 G. K. Madsen, J. Carrete and M. J. Verstraete, *Comput. Phys. Commun.*, 2018, **231**, 140–145.
49 W. Ibarra-Hernández, M. J. Verstraete and J.-Y. Raty, *Phys. Rev. B: Condens. Matter Mater. Phys.*, 2014, **90**, 245204.
50 J. Horak, J. Navratil and Z. Starý, *J. Phys. Chem. Solids*, 1992, **53**, 1067–1072.
51 P. Lošťák, Č. Drašar, D. Bachan, L. Beneš and A. Krejčová, *Radiat. Eff. Defects Solids*, 2010, **165**, 211–215.
52 W. S. Liu, Q. Zhang, Y. Lan, S. Chen, X. Yan, Q. Zhang, H. Wang, D. Wang, G. Chen and Z. Ren, *Adv. Energy Mater.*, 2011, **1**, 577–587.
53 X. Duan and Y. Jiang, *Appl. Surf. Sci.*, 2010, **256**, 7365–7370.
54 Q. Zhang, T. Fang, F. Liu, A. Li, Y. Wu, T. Zhu and X. Zhao, *Chem.–Asian J.*, 2020, **15**, 2775–2792.
55 S. J. Kim, H. Choi, Y. Kim, J. H. We, J. S. Shin, H. E. Lee, M.-W. Oh, K. J. Lee and B. J. Cho, *Nano Energy*, 2017, **31**, 258–263.
56 D. Perrin, M. Chitroub, S. Scherrer and H. Scherrer, *J. Phys. Chem. Solids*, 2000, **61**, 1687–1691.
57 M. Kim, S.-i. Kim, H.-j. Cho, H. Mun, H.-s. Kim, J.-H. Lim, S. W. Kim and K. H. Lee, *Scr. Mater.*, 2019, **167**, 120–125.
58 X. Hu, C. Jiang, Z. Pan, B. Feng, P. Liu, G. Li and Y. Li, *Mater. Res. Express*, 2018, **6**, 035907.

 

59 L. Zhao, B.-P. Zhang, W. Liu, H. Zhang and J.-F. Li, *J. Alloys Compd.*, 2009, **467**, 91–97.
60 J. Yang, T. Aizawa, A. Yamamoto and T. Ohta, *J. Alloys Compd.*, 2000, **312**, 326–330.
61 H.-S. Kim, Z. M. Gibbs, Y. Tang, H. Wang and G. J. Snyder, *APL Mater.*, 2015, **3**, 041506.
62 D. K. Misra, S. Sumithra, N. S. Chauhan, W. Nolting, P. Poudeu and K. L. Stokes, *Mater. Sci. Semicond. Process.*, 2015, **40**, 453–462.
63 Z. Liu, J. Mao, T.-H. Liu, G. Chen and Z. Ren, *MRS Bull.*, 2018, **43**, 181–186.
64 R. Gurunathan, R. Hanus and G. J. Snyder, *Mater. Horiz.*, 2020, **7**, 1452–1456.
65 S. Grasso, N. Tsujii, Q. Jiang, J. Khaliq, S. Maruyama, M. Miranda, K. Simpson, T. Mori and M. J. Reece, *J. Mater. Chem. C*, 2013, **1**, 2362–2367.
66 M. T. Agne, P. W. Voorhees and G. J. Snyder, *Adv. Mater.*, 2019, **31**, 1902980.
67 C. Goupil, *Continuum theory and modeling of thermoelectric elements*, John Wiley & Sons, 2015.
68 G. J. Snyder and T. S. Ursell, *Phys. Rev. Lett.*, 2003, **91**, 148301.
69 G. J. Snyder and T. Caillat, *MRS Online Proceedings Library Archive*, 2003, vol. 793.
70 C. Hadjistassou, E. Kyriakides and J. Georgiou, *Energy Convers. Manage.*, 2013, **66**, 165–172.
71 N. S. Chauhan, S. Bathula, A. Vishwakarma, R. Bhardwaj, K. K. Johari, B. Gahtori, M. Saravanan and A. Dhar, *J. Phys. Chem. Solids*, 2018, **123**, 105–112.
72 Y. Xing, J. Yu, C. Hu, Z. Huang, Q. Qiu, C. Wang, X. Xia, Z. Wang, S. Bai, X. Zhao, L. Chen and T. Zhu, *Adv. Energy Mater.*, 2020, **10**, 2000888.
73 N. S. Chauhan, S. Bathula, B. Gahtori, S. D. Mahanti, A. Bhattacharya, A. Vishwakarma, R. Bhardwaj, V. N. Singh and A. Dhar, *ACS Appl. Mater. Interfaces*, 2019, **11**, 47830–47836.
74 N. S. Chauhan, P. R. Raghuvanshi, K. Tyagi, K. K. Johari, L. Tyagi, B. Gahtori, S. Bathula, A. Bhattacharya, S. D. Mahanti and V. N. Singh, *J. Phys. Chem. C*, 2020, **124**, 8584–8593.
75 B. Zhu, Z.-Y. Huang, X.-Y. Wang, Y. Yu, L. Yang, N. Gao, Z.-G. Chen and F.-Q. Zu, *Nano Energy*, 2017, **42**, 8–16.
76 R. Zhai, L. Hu, H. Wu, Z. Xu, T.-J. Zhu and X.-B. Zhao, *ACS Appl. Mater. Interfaces*, 2017, **9**, 28577–28585.
77 K. Park, K. Ahn, J. Cha, S. Lee, S. I. Chae, S.-P. Cho, S. Ryee, J. Im, J. Lee and S.-D. Park, *J. Am. Chem. Soc.*, 2016, **138**, 14458–14468.
78 F. Hao, T. Xing, P. Qiu, P. Hu, T. Wei, D. Ren, X. Shi and L. Chen, *ACS Appl. Mater. Interfaces*, 2018, **10**, 21372–21380.
79 S. Li, X. Liu, Y. Liu, F. Liu, J. Luo and F. Pan, *Nano Energy*, 2017, **39**, 297–305.
80 J. Zhang, H. Ming, D. Li, X. Qin, J. Zhang, L. Huang, C. Song and L. Wang, *ACS Appl. Mater. Interfaces*, 2020, **12**, 37155–37163.